JACS
JOURNAL OF THE AMERICAN CHEMICAL SOCIETY
pubs.acs.org/JACS
Article

Atomic-Level Structure of Zinc-Modified Cementitious Calcium Silicate Hydrate

Anna Morales-Melgares,[‖] Ziga Casar,[‖] Pinelopi Moutzouri, Amrit Venkatesh, Manuel Cordova, Aslam Kunhi Mohamed, Karen L. Scrivener,* Paul Bowen,* and Lyndon Emsley*

Cite This: J. Am. Chem. Soc. 2022, 144, 22915−22924
Read Online
ACCESS | Metrics & More | Article Recommendations | Supporting Information

ABSTRACT: It has recently been demonstrated that the addition of zinc can enhance the mechanical strength of tricalcium silicates (C_3S) upon hydration, but the structure of the main hydration product of cement, calcium silicate hydrate (C-S-H), in zinc-modified formulations remains unresolved. Here, we combine ^{29}Si DNP-enhanced solid-state nuclear magnetic resonance (NMR), density functional theory (DFT)-based chemical shift computations, and molecular dynamics (MD) modeling to determine the atomic-level structure of zinc-modified C-S-H. The structure contains two main new silicon species ($Q^{(1,Zn)}$ and $Q^{(2p,Zn)}$) where zinc substitutes $Q^{(1)}$ silicon species in dimers and bridging $Q^{(2b)}$ silicon sites, respectively. Structures determined as a function of zinc content show that zinc promotes an increase in the dreierketten mean chain lengths.

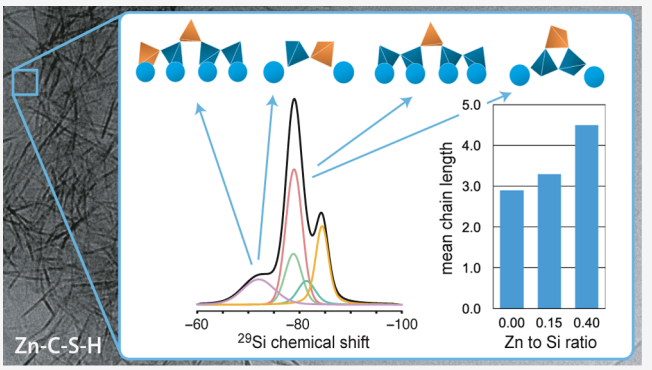

INTRODUCTION

Due to it being the second most used substance on earth (after water), concrete accounts for around 8% of anthropogenic CO_2 emissions.[1] The most promising approach to lower this carbon footprint is the partial substitution of clinker by supplementary cementitious materials (SCMs) such as fly ash, blast furnace slag, limestone, and calcined clays. The SCMs have much lower associated CO_2, but blending them with clinker tends to lower the early-age strength of the resulting concrete.[2,3] This means that increasing the reaction rate of cement formation would allow higher substitution levels and lower CO_2 emissions.

It has been demonstrated that the addition of zinc to C_3S or alite (the main phase in clinker) can enhance the 1-day mechanical strength of the hydrated paste substantially (×3).[4−6] This accelerated strength development is related to the faster growth of longer and thicker calcium silicate hydrate (C-S-H) particles, which is the main phase (around 50% by volume) in the cement paste part of the final hardened concrete.[7−9] Ouzia and Scrivener[10] demonstrated that C-S-H nucleates and grows predominantly as outgrowths on the surface of alite grains during the hardening reaction (hydration). The rate of reaction peaks at about 10 h (at 20 °C). After this, the reaction rate drops to a low rate at 1 day as the period of fast growth of C-S-H ends. Small amounts of zinc oxide in alite were found to enhance the heat flow and the degree of hydration, and they also result in longer and thicker outgrowths of C-S-H.[11] There is a concomitant enhancement of compressive strength of concrete during the early stages of hardening for up to 7 days.[5] Although zinc addition could potentially increase the overall cost of cement, understanding the role of zinc in C-S-H growth and kinetics would open pathways to synthetic tunability of the rate of reaction of lower-CO_2 materials. However, the atomic-level mechanism of action that links the presence of small amounts of zinc to the enhanced growth of C-S-H, and so to the faster development of strength, is not known. Therefore, it would be of great value to determine how zinc is incorporated into the C-S-H structure at the atomic level.

A number of techniques have been used previously to probe the structure of C-S-H,[12−14] but interpretation is hampered by the lack of long-range order. Indeed, the atomic-level structure of C-S-H materials with industrially relevant Ca/Si ratios (i.e., higher than 1.5) was only determined recently[15,16] by the use of a combination of solid-state NMR spectroscopy, molecular dynamics, and density functional theory (DFT)-based chemical shift calculations.

Here, we determine the atomic-level structure of zinc-modified synthetic C-S-H using dynamic nuclear polarization

Received: June 27, 2022
Published: December 12, 2022

https://doi.org/10.1021/jacs.2c06749
J. Am. Chem. Soc. 2022, 144, 22915−22924

(DNP)-enhanced solid-state NMR spectroscopy in concert with other standard characterization methods. Notably, we discover that the structure contains new silicate species that are directly related to the incorporation of zinc and have not been observed previously to the best of our knowledge. We also find that increasing zinc content leads to increasing silicate chain lengths in the structure, which is concomitant with the observed increase in the length of the C-S-H outgrowths at the meso-scale.

METHODS

Synthesis. Samples were synthesized through the dropwise precipitation method previously developed by Kumar et al.[15] and standardized by Harris et al.[17] A polymethacrylate batch reactor was placed in a water bath to maintain a temperature between 19 and 21 °C. Two hundred milliliters of a 50 mM sodium silicate solution in deionized water was placed in a batch reactor and 5 mL of 10 M NaOH was added to regulate the final pH between 12.8 and 13.0 to ensure a target Ca/Si molar ratio of ∼1.75. The two solutions were mixed and purged under a flow of nitrogen gas for 15 min prior to the reaction. Two hundred milliliters of 90 mM calcium nitrate tetrahydrate (and zinc nitrate hexahydrate with varying concentrations depending on the target $(Zn/Si)_i$) was added through a piston pump at a rate of 2 mL/min followed by stirring at 1100 rpm for 3 h after which the precipitate was collected, washed with 60 mL of a 50% ethanol/water solution, and filtered under vacuum. The supernatant of each sample was also collected. The amounts of reactants used for each sample can be found in Table S1 in the Supporting Information (SI).

X-ray Diffraction (XRD). Powder XRD was performed on a qualitative basis to observe the presence of undesired phases (i.e., portlandite).[18] The main C-S-H peaks appear at 29.4, 32.1, and 50.1 ± 0.1°.[19] A Bruker Discovery X-ray diffractometer with double bounced monochromatic CuK α radiation (λ = 1.54 Å) was used. A fixed divergence slit of 0.25 mm was used and the experimental time for all samples was 30 min. Spectra and further details are given in SI Section IIa.

Inductively Coupled Plasma (ICP). Samples were prepared by dispersing 20 mg of C-S-H gel or 1 mL of the supernatant in 10 mL or 9 mL of concentrated nitric acid, respectively. Then, the samples were diluted up to three orders of magnitude prior to analysis. Experiments were conducted using a Spectro Arcos ICP-OES analyser from Ametek. Further details are given in SI Section IIc.

Electron Microscopy. A Tecnai OSIRIS TEM system at 200 kV in bright field mode with a single tilt holder and FEI SmartCAM CCD camera was used to observe the sample morphology (SI Section IIb). The TEM grids employed to observe these samples are copper-based grids coated with a thin film of carbon. C-S-H gel (100−300 mg) was dispersed in ca. 20 mL of isopropanol (IPA). The samples were dried prior to analysis.

Electron Dispersive X-rays (EDX). The same instrument used for TEM analysis was used to conduct STEM and STEM-EDX experiments. In STEM mode, a bright field (BF) detector and a high-angle annular dark-field (HAADF) detector were used, whereas in EDX mode, a twin pole piece with a Super-X EDX system and four SDD detectors with a 0.9 rad solid angle were used.

NMR Spectroscopy. Samples were prepared for DNP-enhanced NMR[20−22] by adapting previously used protocols for C-S-H materials.[15,16] About 300 mg of the C-S-H gel was mixed with 3 mg of AMUPol[23] and dried under N_2 flow to ∼200 mg before packing into sapphire rotors and sealing with PTFE inserts and zirconia drive caps. Since the poorly crystalline C-S-H structure contains a substantial amount of water that is not all removed, no additional impregnating medium is required.[15] All experiments were performed using a 400 MHz Bruker Avance III HD NMR spectrometer equipped with a 263 GHz Bruker gyrotron[24] or klystron microwave source and a HXY 3.2 mm low-temperature MAS DNP probe in $^1H-^{29}Si$ configuration at 100 K. ^1H DNP enhancements were measured as the ratio of the $^1H\rightarrow^{29}Si$ cross-polarization (CP) signal intensity between spectra recorded with and without microwaves and were found to be between 30 and 40. All spectra were acquired at a magic angle spinning (MAS) frequency of 8 kHz, except for SUPER[25] and 2D spin diffusion experiments, which were performed at 5 kHz. For multi-CPMAS experiments, presaturation pulse trains were applied on ^1H and ^{29}Si channels. The ^{29}Si chemical shifts were referenced to tetrakis (trimethylsilyl)silane (TMSS). Topspin was used to acquire and process NMR spectra, while fitting of the chemical shift anisotropy patterns was performed with ssNake.[26] Additional experimental details are provided in the SI.

Atomistic Structure Modeling. The previously reported brick model was used to generate candidate zinc-modified C-S-H structures.[27] LAMMPS[28] was used for structure energy minimization and the Erica FF2[29] force field extended with the required zinc interatomic potentials[30] was used. A single or double brick unit cell was constructed with a target Ca/(Si+Zn) ratio while maintaining the characteristic features of the C-S-H structure.[15] Some silicate tetrahedra were replaced with zinc polyhedra including four-coordinate ZnO_4^{6-} and $ZnO_2(OH)_2^{4-}$ and five-coordinate $ZnO_2(OH)_3^{5-}$ species. To achieve charge balance, the number of interlayer calcium ions (Ca^{2+}) and hydroxides (OH^-) were adjusted. Classical energy minimization with the Erica FF2 force field was carried out prior to the DFT energy minimization to discard energetically unfavorable structures and save computational time. Full details and codes used are provided with the raw data.

Chemical Shift Computations. The atomic positions and lattice parameters of the structures obtained from molecular dynamics modeling were first optimized using the Perdew−Burke−Ernzerhof (PBE)[31] functional and Grimme D2 dispersion correction.[32,33] Projector augmented wave scalar relativistic pseudopotentials obtained from PSlibrary version 1.0.0 were used.[34,35] Semicore s and p electrons were included for zinc and calcium, and nonlinear core correction was applied for heavy atoms. Wavefunction and charge density energy cutoffs were set to 160 and 1280 Ry, respectively. A Monkhorst−Pack grid of k-points corresponding to a maximum spacing of 0.05 $Å^{-1}$ was used.[36] After geometry optimization, a single-point computation was performed with the same parameters, and chemical shieldings were computed using the GIPAW method.[37,38]

The conversion from computed shieldings (σ) to ^{29}Si chemical shifts (δ) was carried out by linear regression ($\delta = -1.05\sigma + 345.32$) using a reference set of crystal structures containing willemite,[39] hemimorphite,[40] foshagite,[41] and α-quartz[42] with their corresponding experimental shifts.[43,44] All NMR computations were carried out using the plane-wave DFT program Quantum ESPRESSO v6.5.[45,46] Simulated ^{29}Si spectra for individual Si sites were generated using a kernel density estimate of Gaussian kernels as implemented in the scipy Python library.[47]

RESULTS AND DISCUSSION

Chemical Composition and Morphology. As described previously, single-phase C-S-H can be synthesized using a dropwise precipitation method, which allows for a controlled synthesis of C-S-H with a specific Ca/Si ratio.[17] This approach was modified to produce zinc-modified C-S-H by adding certain amounts of zinc nitrate hexahydrate to the aqueous calcium nitrate solution depending on the target Zn to Si ratio (denoted as $(Zn/Si)_i$ where the subscript i indicates that it is the initial ratio used in the synthesis). The initial calcium and zinc nitrate solution had calcium concentration of 90 mM and zinc concentration of 0, 7.5, or 20 mM depending on their target $(Zn/Si)_i$ (e.g., 0, 0.15, and 0.40, respectively). The initial sodium metasilicate solution had a concentration of 50 mM.

As described by Anseau et al.,[48] both zinc and aluminum can form complexes with silicate monomers, which are the main species in solution at the pH used here. Therefore, zinc is expected to behave similar to aluminum and to substitute for

https://doi.org/10.1021/jacs.2c06749
J. Am. Chem. Soc. 2022, 144, 22915−22924

silicate species, as seen in the case of aluminum incorporation in C-A-S-H structures synthesized through dropwise precipitation.[16] In addition, previous studies on C_3S hydration in the presence of zinc show that zinc is in tetrahedral coordination and substitutes for silicate species in C-S-H chains.[49,50] DFT-relaxed structures in which zinc substituted for calcium in the main layer presented 6-fold coordination and unusually long bond lengths (see SI Section VII); therefore, substitution of main layer calcium by zinc was neglected.

The possible sites where different zinc polyhedra can be incorporated into the C-S-H structure (Figure 1A) are

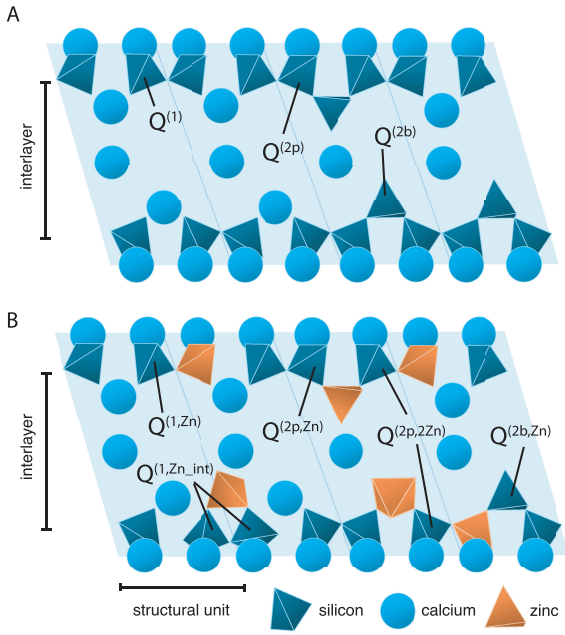

Figure 1. (A) Schematic of the dreierketten chains in conventional C-S-H showing all of the silicate species present: $Q^{(1)}$, $Q^{(2b)}$, and $Q^{(2p)}$. (B) Schematic of zinc-modified C-S-H, showing all of the new silicate sites that could potentially be present: $Q^{(1,Zn)}$, $Q^{(2p,Zn)}$, $Q^{(2p,2Zn)}$, $Q^{(2b,Zn)}$, and $Q^{(1,Zn\_int)}$.

illustrated in Figure 1B. These structures are a result of zinc substitutions of $Q^{(2b)}$, $Q^{(2p)}$, or $Q^{(1)}$ sites in conventional C-S-H. In addition, the figure also shows how zinc can also be present on top of the silicate chains, facing into the interlayer, where it could coordinate to one or both $Q^{(1)}$ species of a silicate dimer.

If zinc substitutes for the $Q^{(2b)}$ site, it yields two identical new neighboring silicate species, which, following the Q-site nomenclature, are named $Q^{(2p,Zn)}$. If zinc substitutes for a $Q^{(2p)}$ site, it yields a $Q^{(2b,Zn)}$ species and either a $Q^{(1,Zn)}$ or a $Q^{(2p,Zn)}$ depending on whether the chain unit is a pentamer or a higher-degree unit, respectively. If zinc substitutes for a $Q^{(1)}$ site it can yield a $Q^{(1,Zn)}$ or a $Q^{(2p,Zn)}$, depending on whether the chain unit is a dimer or a higher-degree unit. If zinc is adjacent to both silicates in a $Q^{(1)}$–$Q^{(1)}$ dimer, it coordinates to one or both $Q^{(1)}$ species and protrudes into the interlayer, becoming a $Q^{(2p,Zn\_int)}$. Finally, this model also includes the possibility of two zinc units substituting for two silicate chain sites simultaneously (i.e., $Q^{(1)}$ and $Q^{(2p)}$), producing a new silicate species that is isolated from other silicate linkages, as represented in Figure 1B in the case of $Q^{(2p,2Zn)}$ species.

In summary, this scheme includes the possibility of five different four-coordinated zinc species and one five-coordinated zinc species substituting for a $Q^{(2b)}$ site.

To determine the atomic-level structure of zinc-modified C-S-H, the chemical composition, purity, and incorporation of zinc in the C-S-H structure need to be verified prior to structure determination. A series of XRD experiments were performed to confirm that our material is a single-phase, pure C-S-H sample and no secondary phases such as portlandite are observed (Figure S1). Additionally, inductively coupled plasma (ICP) analysis of the supernatant shows that only around 1–2% of the added zinc remains in solution after synthesis (Table S2), indicating the incorporation of the vast majority of zinc into the precipitated zinc-modified C-S-H.

Figure 2A shows normalized EDX spectra of samples with different initial Zn to Si ratios of 0.03, 0.08, and 0.15 in the

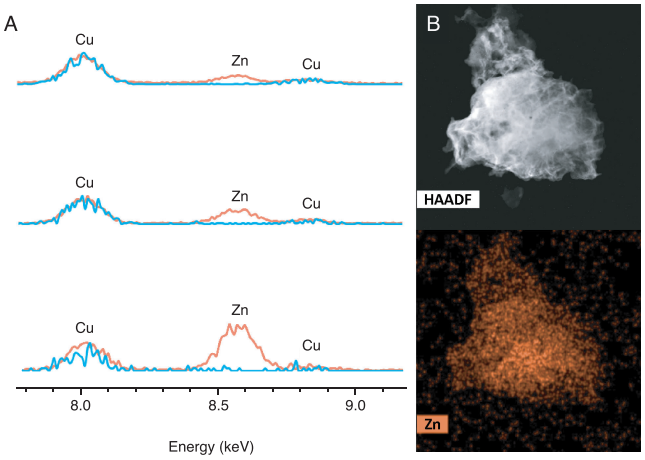

Figure 2. (A) STEM-EDX spectra of C-S-H samples with $(Zn/Si)_i$ ratios of 0.03 (top), 0.08 (center), and 0.15 (bottom). For each $(Zn/Si)_i$, spectra corresponding to regions including (orange) and excluding (blue) C-S-H particles are shown. The intensities of the Zn signals are normalized with respect to the Cu absorption line at 8 keV from the TEM grid. (B) HAADF-STEM X-ray composition map of a C-S-H particle with a $(Zn/Si)_i$ ratio of 0.15, showing an apparent Zn uptake.

reagent solutions. Comparison of the EDX spectra recorded from a region excluding (blue) and including a C-S-H particle (orange) shows a clear trend: samples that have been synthesized with an increased concentration of zinc nitrate show higher zinc counts in the EDX experiment, pointing to an incorporation of zinc in C-S-H (Figure 2A). Furthermore, HAADF and TEM data show no appreciable differences between the observed morphology of conventional C-S-H and zinc-modified C-S-H, with all samples showing a nanofoil morphology that is consistent with the literature (Figures 2B and S2).

Characterization by DNP NMR. To determine the zinc-modified C-S-H structure, DNP-enhanced ^{29}Si one-dimensional (1D) multi-CPMAS NMR spectra[51] and two-dimensional (2D) INADEQUATE spectra[15,22,52,53] were obtained.

To be able to acquire the relatively insensitive 1D and 2D ^{29}Si solid-state spectra necessary to determine the populations and connectivities of different silicon sites in the materials, we prepared a series of zinc-modified C-S-H formulations. These were chosen to yield enhancement of NMR signals by MAS DNP,[20,21] by adapting the procedures developed previ-

https://doi.org/10.1021/jacs.2c06749
J. Am. Chem. Soc. 2022, 144, 22915–22924

ously[15,16,20] by incorporating a small amount of the organic biradical AMUPol[23] into the C-S-H sample. When the sample is frozen at 100 K, AMUPol allows efficient transfer of large electron polarization to protons in the frozen sample when microwaves are applied. The enhanced ^{1}H magnetization is then transferred to ^{29}Si nuclei through CP.

Figure 3A compares the ^{29}Si DNP-enhanced multi-CP spectra from three samples with $(Zn/Si)_i$ of 0, 0.15, and 0.40. The multi-CPMAS pulse sequence, which is based on the repetition of CP periods,[51] yields ^{29}Si NMR spectra that allow for quantitative analysis of different silicate species in C-S-H samples.[51,54] The spectrum of the sample with $(Zn/Si)_i$ of 0 shows the well-characterized ^{29}Si peaks expected in conventional high Ca/Si ratio C-S-H whose signals are attributed to $Q^{(1)}$ (−78.9 ppm), $Q^{(2b)}$ (−81.4 ppm), and $Q^{(2p)}$ (−84.4 ppm) silicate species.[15,55−57] The spectra of the samples with $(Zn/Si)_i$ of 0.15 and 0.40 show the presence of new Q sites at around −72 and −79 ppm; details regarding the spectral deconvolution are provided below. All of the different species present in the zinc-modified C-S-H spectra are more clearly shown in Figure 3B where the deconvolution of different Q sites is carried out. The presence of the new ^{29}Si signals around −72 and −79 ppm suggests the incorporation of zinc in the C-S-H structure as it indicates that the chemical environment of at least one silicate species is changed with respect to conventional C-S-H samples. The new species that gives rise to the signal at −72 ppm has a chemical shift similar to those of silicate monomers ($Q^{(0)}$) that typically range from −60 to −75 ppm.[58] Silicate monomers ($Q^{(0)}$) are however discarded since, although observed in minor amounts in works from other groups with different synthetic routes,[59−61] they are not usually observed in C-S-H samples,[15,16] and they are not a characteristic feature of the high Ca/Si ratio C-S-H structures synthesized through our dropwise precipitation method.[15,16]

The spectra in Figure 3A were normalized to total intensity and show evidence of two trends. As the $(Zn/Si)_i$ is increased, the signal at −78.9 ppm decreases while the new signal at around −72 ppm increases in intensity. To further investigate the species present, DNP-enhanced natural-abundance homonuclear ^{29}Si−^{29}Si refocused INADEQUATE spectra were acquired.[15,22,52,53] A 2D INADEQUATE spectrum of a zinc-modified C-S-H gel with $(Zn/Si)_i$ of 0.40 is shown in Figure 3C (and spectra corresponding to $(Zn/Si)_i$ of 0 and 0.15 are shown in SI Section Vb).

This spectrum shows the expected connectivities in conventional C-S-H samples:[15] $Q^{(1)}$−$Q^{(1)}$, $Q^{(2p)}$−$Q^{(1)}$, $Q^{(2p)}$−$Q^{(2b)}$, and $Q^{(2p)}$−$Q^{(2p)}$. Signals corresponding to $Q^{(2b)}$−$Q^{(1)}$ or $Q^{(2b)}$−$Q^{(2b)}$ connectivities are not present, as is consistent with the connectivity of the C-S-H silicate chains. Additionally, no correlations with the new ^{29}Si species at −72 ppm are observed. Through-space exchange spectroscopy (EXSY) experiments were also carried out and confirmed that this new species, although not having through-bond correlations with other Q sites, has close through-space correlations mediated by spin diffusion, which further confirms its incorporation in the C-S-H internal structure. Results from the ^{29}Si−^{29}Si EXSY experiments are shown in Figures S9 and S10.

Candidate Structure Generation: Stability of Zincate Species in Zinc-Modified C-S-H. To determine the possible sites for incorporation of zinc species into the silicate chains of C-S-H at the atomic level, 98 different zinc-modified C-S-H structural units with Ca/Si ratios ranging from 1.2 to 2.25 were

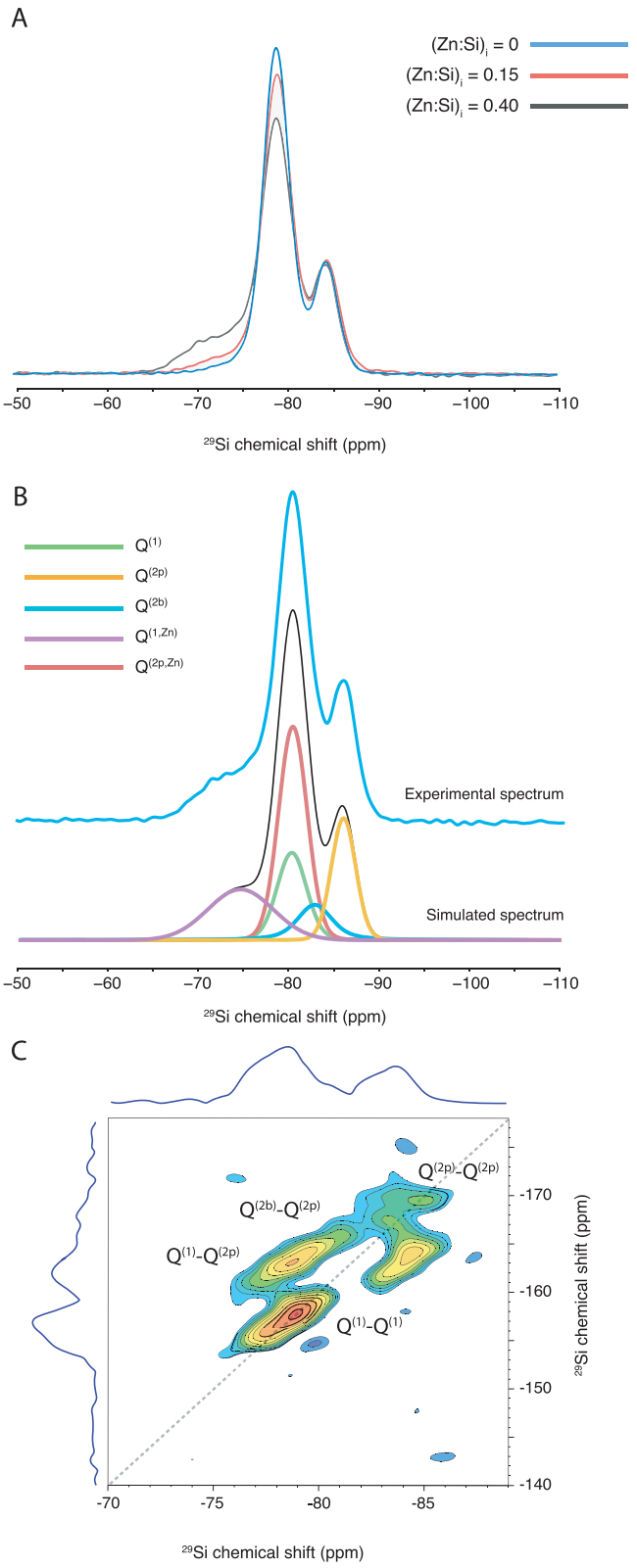

Figure 3. DNP-enhanced (A) ^{29}Si{^{1}H} 1D multi-CPMAS spectra of samples with $(Zn/Si)_i$ of 0, 0.15, and 0.40; (B) 1D multi-CPMAS spectrum of the sample with $(Zn/Si)_i$ of 0.40 (top) showing deconvolution into the different Q sites (bottom); and (C) 2D ^{29}Si−^{29}Si INADEQUATE spectrum of a zinc-modified C-S-H sample with a $(Zn/Si)_i$ ratio of 0.40.

https://doi.org/10.1021/jacs.2c06749
J. Am. Chem. Soc. 2022, 144, 22915−22924

generated via brick models.[27] For each structure, DFT[32,34]-based chemical shifts were calculated and compared to the experimental chemical shifts obtained from 1D and 2D NMR experiments. To calibrate the calculated shifts, the mean shifts of the well-established characteristic sites present in conventional C-S-H gels ($Q^{(1)}$, $Q^{(2p)}$, $Q^{(2b)}$) were computed (Figure 4B) and found to be in good agreement with experiments and literature. All possible DFT-based calculated chemical shifts for all of the silicon sites in the 98 candidate structures are provided with the raw data.

DFT was also used to compute the absolute energies of each structure to investigate differences in stability. Figure 4A shows a selection of relevant structures, where four-coordinated zinc substitutes for $Q^{(1)}$, $Q^{(2p)}$, or $Q^{(2b)}$ silicates or is adjacent to two silicates and in the interlayer. The calculated energies of all candidate structures corresponding to a Ca/Si ratio of 1.67 and 2.0 are shown in Figure S4. Table S3 shows the relative calculated energies of all of the candidate structures, ordered in sets according to their Ca/Si ratio. The calculated energies are normalized to the structure where zinc substitutes for a $Q^{(2b)}$ site and is coordinated as $ZnO_2(OH)_2$, which is consistently the most stable Q-site substitution at Ca/Si ratios of 1.67.

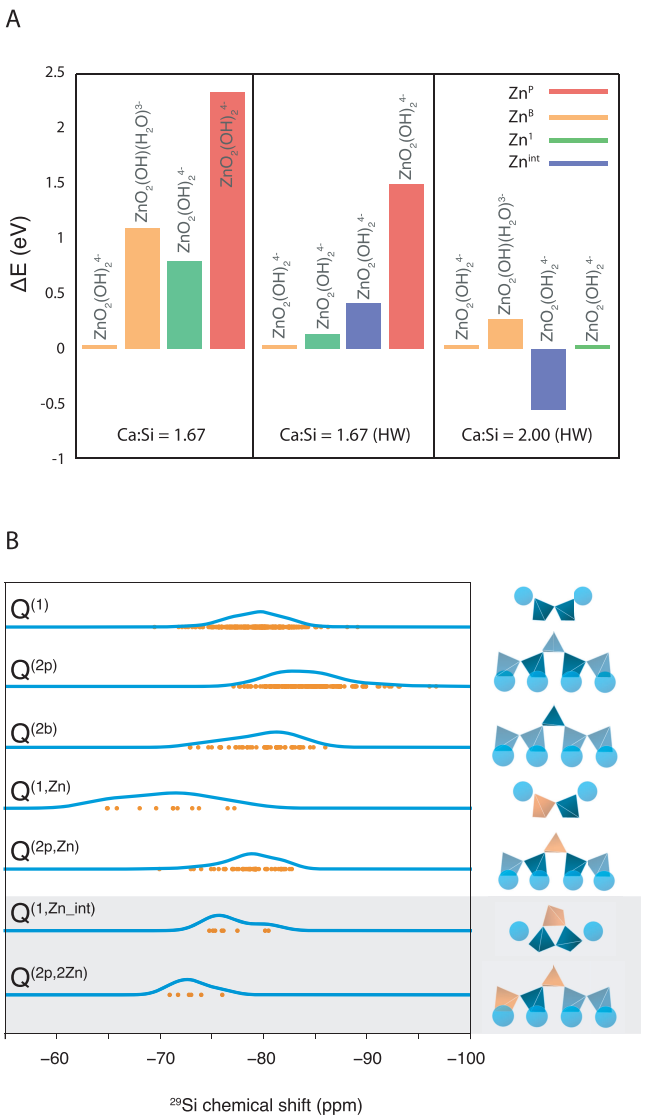

Figure 4. (A) Relative calculated energies of representative zinc-modified C-S-H structures according to each substitution site with different Ca/Si ratios and interlayer amounts. Each column is normalized to the substitution of zinc in the bridging site with $\Delta E = 0$ eV. Nomenclature: Zn^B = zinc in the $Q^{(2b)}$ site, Zn^P = zinc in the $Q^{(2p)}$ site, Zn^1 = zinc in the $Q^{(1)}$ site, Zn^{Int} = zinc on top of a $Q^{(1)}$–$Q^{(1)}$ dimer site, and HW = high water content. All structures are labeled with their corresponding zinc species that may coordinate to hydroxides or water. (B) DFT-calculated shifts from the silicate species obtained from brick models for zinc-modified C-S-H and their respective schematic structures.

NMR Crystallography with DFT-Based Calculated Chemical Shifts. The DFT-calculated ^{29}Si isotropic shifts resulting from each structure are shown in Figures 4B and S5 and also provided with the raw data. Results from energy minimization and chemical shift calculations through DFT were then compared to experimental data from both 1D multi-CPMAS and 2D INADEQUATE experiments to verify or discard the relaxed structures, as discussed below.

At the Ca/Si ratios used in this work, zinc substituting for a $Q^{(2b)}$ site is predicted to be the most favorable structure owing to its lowest mean energies, while zinc substituting for a $Q^{(1)}$ site is predicted to be energetically more favorable than zinc substituting for a $Q^{(2p)}$ site (Figure S4). This is consistent with the experimental 2D ^{29}Si–^{29}Si INADEQUATE NMR results, since zinc substitution in a $Q^{(2p)}$ site should yield $Q^{(2b,Zn)}$–$Q^{(2p)}$ and $Q^{(2b,Zn)}$–$Q^{(2p,Zn)}$ correlations in the region between −74.8 and −84.4 ppm, which are not observed. Based on both the calculated energies and the NMR results, we conclude that zinc does not substitute for the $Q^{(2p)}$ species in C-S-H.

When zinc substitutes for a $Q^{(1)}$ site in a dimer, the mean calculated isotropic chemical shift of the generated $Q^{(1,Zn)}$ species, as shown in Figure 4B, is −71.5 ppm that is also the measured value for a Zn–Si dimer complex.[48] This value agrees with the signal observed experimentally at approximately −72 ppm and is also consistent with the fact that there are no ^{29}Si–^{29}Si correlations with this chemical shift in the 2D INADEQUATE NMR experiments. Additionally, our DFT calculations predict a lower span (Ω) of the chemical shift anisotropy (CSA) tensor for $Q^{(1,Zn)}$ when compared to the other species, which is in agreement with our experimental results (see SI Section Vd).

Having unambiguously identified the $Q^{(1,Zn)}$ species, we however note that it can only account for ca. 60–70% of the total zinc content (see SI Section Ve). Therefore, the remaining zinc atoms must be incorporated in other sites of the structure.

In all of the 1D multi-CPMAS spectra with the $(Zn/Si)_i$ ratio between 0 and 0.4, the ratios of the integrated signal intensities of $Q^{(2p)}$ and $Q^{(2b)}$ sites are found to be consistently equal to two, as expected. Upon inclusion of a fifth site in the deconvolution of the ^{29}Si NMR spectra with a signal intensity constrained to account for the remaining 30–40% of zinc, the only possible chemical shift for the second new ^{29}Si species is found to be −79 ppm (Figure 3B).

With DFT, substitution for $Q^{(2b)}$ is always predicted to be the most favorable energetically at Ca/Si ratio 1.67 (Table S3), and the resulting two symmetrical ^{29}Si sites, denoted $Q^{(2p,Zn)}$, have a calculated mean chemical shift of −79 ppm.

Due to the overlap of the $Q^{(2p,Zn)}$ species with the $Q^{(1)}$ species (−78.9 ppm), these two species are indistinguishable in 1D ^{29}Si NMR spectra. The $Q^{(2p,Zn)}$ species can be connected either to $Q^{(2p)}$ or $Q^{(1)}$ species, which would yield similar correlations as those observed between $Q^{(1)}$–$Q^{(1)}$ and $Q^{(2p)}$–

https://doi.org/10.1021/jacs.2c06749
J. Am. Chem. Soc. 2022, 144, 22915−22924

$Q^{(1)}$ species, making them again indistinguishable in the INADEQUATE spectra. However, we note that the only substitution site that is compatible with both the 1D multi-CPMAS and 2D INADEQUATE experiments is $Q^{(2b)}$, leading to two symmetrical $Q^{(2p,Zn)}$ species. These considerations, taken together with the fact that the integrated area corresponding to the conventional $Q^{(2p)}$ sites cannot account for all of the expected new species arising from zinc incorporation, led us to determine that the only region where the signal corresponding to $Q^{(2p,Zn)}$ species could be is indeed overlapping with the signal that corresponds to the $Q^{(1)}$ species. Therefore, we assign a second new ^{29}Si species at −79 ppm to be $Q^{(2p,Zn)}$. The substitution at the bridging site is also analogous to the previously determined C-A-S-H structure.[16]

Based on the evidence shown, $Q^{(1,Zn)}$ and $Q^{(2p,Zn)}$ species are identified as the main silicate species arising from zinc incorporation in C-S-H systems.

Finally, we consider two other energetically possible sites $Q^{(2p,2Zn)}$ and $Q^{(1,Zn\_int)}$ (see Figure 4B). $Q^{(2p,2Zn)}$ species (Figure 1), with a calculated chemical shift of −73.0 ppm, can only be present in a pentamer or a higher-degree unit if zinc substitutes for the $Q^{(1)}$ and $Q^{(2b)}$ species simultaneously, creating a Zn−Si−Zn linkage at the start of the chain. The calculated chemical shift is similar to that of $Q^{(1,Zn)}$ species and would yield a signal in the 1D ^{29}Si experiments while yielding no ^{29}Si−^{29}Si correlations in the 2D ^{29}Si INADEQUATE NMR experiments, which is compatible with our results. This species requires a high $(Zn/Si)_i$ as well as a high degree of polymerization to occur, as it is the combination of a zinc substitution for $Q^{(1)}$ and $Q^{(2b)}$ simultaneously. Due to the fact that this species ($Q^{(2p,2Zn)}$) requires two Zn substitutions to occur, though possible, they are rendered less probable and are discarded in further analysis.

$Q^{(1,Zn\_int)}$ (Figure 1) has a calculated chemical shift at around −75 ppm, which would overlap with the signal from $Q^{(1)}$ species. Similarly to $Q^{(2p,Zn)}$ species, $Q^{(1,Zn\_int)}$ species would also be unresolvable in ^{29}Si−^{29}Si INADEQUATE NMR experiments since their predicted correlation would overlap with the $Q^{(1)}$−$Q^{(1)}$ correlation. However, to our knowledge, there are no known structures that exhibit such a Zn−Si feature. Therefore, again, though possible, this species is not considered further.

A summary of the predicted silicate species that arise from zinc incorporation into C-S-H and their DFT-calculated chemical shift distributions is shown in Figure 4B. Our experimental results identify that zinc-modified C-S-H includes $Q^{(1)}$, $Q^{(2p)}$, $Q^{(2b)}$, $Q^{(1,Zn)}$, and $Q^{(2p,Zn)}$, and while $Q^{(2p,2Zn)}$ and $Q^{(1,Zn\_int)}$ species are predicted to be feasible with regard to the energetics, they cannot be verified through ^{29}Si NMR experiments and no such species have been found in the literature, they are therefore shown in Figure 4B as possible structures but they are discarded for the following C-S-H chain length and Q population analyses.

Chain Length and Population Analysis. Quantitative analyses of Q species populations and C-S-H chain length distributions were carried out assuming the silicate species present in zinc-modified C-S-H samples are $Q^{(1)}$, $Q^{(2b)}$, $Q^{(2p)}$, $Q^{(1,Zn)}$, and $Q^{(2p,Zn)}$.

The spectra acquired from samples with $(Zn/Si)_i$ of 0, 0.15, and 0.40 were analyzed by fitting each of the constituent Q sites with a Gaussian lineshape whose integrals are used to determine the relative populations of Q species in each sample (Figure 5). As mentioned above, at a $(Zn/Si)_i$ ratio of 0 (conventional C-S-H), typical ^{29}Si signals for C-S-H with high Ca/Si ratios are present: $Q^{(1)}$ at −78.9 ppm, $Q^{(2b)}$ at −81.4 ppm, and $Q^{(2p)}$ at −84.4 ppm. The population analysis from multi-CPMAS matches the results of Kumar et al.[15] for pure single-phase C-S-H samples with Ca/Si ratios of 1.75.

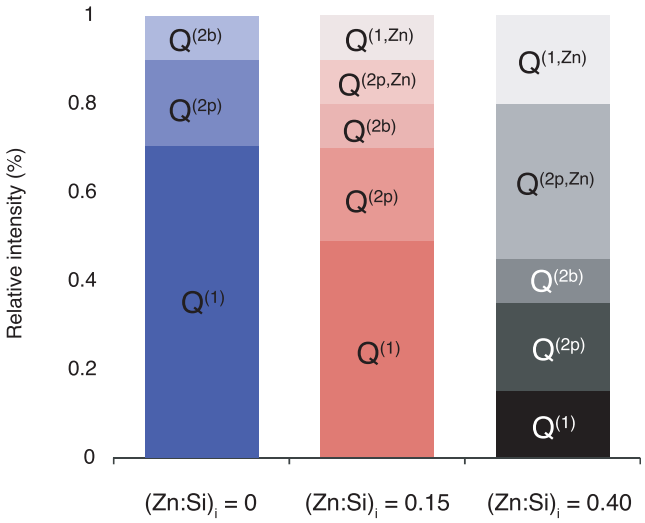

Figure 5. Results of the quantitative population analysis in the three samples with $(Zn/Si)_i$ of 0, 0.15, and 0.40.

Figure 5 shows a quantitative Q species population analysis of the three samples with different $(Zn/Si)_i$ ratios. These results show that conventional C-S-H has a population distribution in which the majority (70%) of the silicate species are $Q^{(1)}$ sites, which is consistent with the literature for high Ca/Si ratios, while 20% are $Q^{(2p)}$ sites and 10% are $Q^{(2b)}$ sites. As zinc is incorporated into the C-S-H structure, the population of $Q^{(1)}$ species decreases, while the populations of $Q^{(2p)}$ and $Q^{(2b)}$ species remain constant. The populations of $Q^{(1,Zn)}$ and $Q^{(2p,Zn)}$ increase upon zinc incorporation. $Q^{(1,Zn)}$ species constitute 10% of all silicate species in samples with $(Zn/Si)_i$ of 0.15, while constituting 23% of all silicate species in the sample with $(Zn/Si)_i$ of 0.40. The $Q^{(2p,Zn)}$ species increases from 10% in the sample with $(Zn/Si)_i$ of 0.15 to 34% in the sample with $(Zn/Si)_i$ of 0.40. This analysis suggests a conversion of $Q^{(1)}$ species into $Q^{(1,Zn)}$ and $Q^{(2p,Zn)}$ species as more zinc is incorporated into the C-S-H structure.

The effect of zinc on the Q-site populations can be related to changes in the distribution of mean chain lengths. Understanding the effect of zinc on the mean chain length distributions could allow for a fine tunability of this material for its implementation at a macroscopic scale. To assess the chain length distribution of zinc-modified C-S-H, it is again assumed that the only species present in the material are $Q^{(1)}$, $Q^{(2p)}$, $Q^{(2b)}$, $Q^{(1,Zn)}$, and $Q^{(2p,Zn)}$. Integrals from the multi-CPMAS population analysis can be combined with the 2D connectivities seen in the INADEQUATE spectra to estimate the molar fractions of dimers in the system following the approach of Kumar et al.,[15] as described in SI Section Vf. Removing SiO_2 units from bridging sites creates defects that shorten and break the chains, generating dimers (x_0), pentamers (x_1), octamers (x_2), and higher-degree units with increasing numbers of SiO_2 bridging sites (x_n). The extent of defects determines the mean chain length, as well as its distribution into dimers, pentamers, octamers, or longer silicate−zincate units. The chain lengths for each sample are

https://doi.org/10.1021/jacs.2c06749
J. Am. Chem. Soc. 2022, 144, 22915−22924

estimated by calculating the molar fractions of $Q^{(1)}$–$Q^{(1)}$ and $Q^{(1)}$–$Q^{(1,Zn)}$ dimers (x_0) and deriving the molar fraction of the silicate–zincate species that have higher degrees of polymerization (x_n).

Table 1 shows the molar fractions of the three samples with different $(Zn/Si)_i$ ratios. The molar fraction of the higher-degree units (x_n), which is a direct sign of a higher degree of polymerization, is lowest in the pure C-S-H sample with $(Zn/Si)_i = 0$. The molar fraction of higher-degree units increases to 0.52 in the sample with $(Zn/Si)_i = 0.15$ and to 0.62 in the sample with $(Zn/Si)_i = 0.40$.

Table 1. Molar Fractions of Dimers (x_0), Higher-Degree Units (x_n), and Mean Chain Length (MCL) for Samples with $(Zn/Si)_i$ of 0, 0.15, and 0.40

$(Zn/Si)_i$ ratio	x_0	x_n	MCL
0.00	0.86	0.14	2.9
0.15	0.48	0.52	3.3
0.40	0.38	0.62	4.5

In addition to the molar fractions of dimers and higher-degree units present in zinc-modified C-S-H, the mean chain length (MCL) of each system was calculated. MCL is calculated according to eq 1 below[27]

$$\mathrm{MCL} = \frac{\text{total Si + Zn species}}{0.5(\text{non bridging species}) - (\text{bridging species})} \quad (1)$$

The MCL of the conventional C-S-H sample (with $(Zn/Si)_i = 0$) is 2.9, and is consistent with the literature for high Ca/Si ratios.[27] The sample with $(Zn/Si)_i = 0.15$ has a calculated MCL of 3.3, and the sample with $(Zn/Si)_i = 0.40$ has a MCL of 4.5. This shows that the presence of $Q^{(2p,Zn)}$ species in zinc-modified C-S-H systems leads to increased MCL with respect to unmodified C-S-H. We conclude that zinc-modified C-S-H has a higher degree of polymerization when compared to conventional C-S-H.

Figure 6 shows a representative atomic-level structure of the zinc-modified C-S-H determined here. It has the characteristic C-S-H $Q^{(1)}$ (−78.9 ppm), $Q^{(2p)}$ (−81.4 ppm), and $Q^{(2b)}$ (−84.36 ppm) species, as well as the newly discovered $Q^{(1,Zn)}$ and $Q^{(2p,Zn)}$ species, and in this example, the $(Zn/Si)_i$ is 0.15. Additional representative structures that incorporate the DFT-predicted $Q^{(1,Zn\_int)}$ and $Q^{(2p,2Zn)}$ species are shown in SI Section VI.

Formation of Zinc-Modified C-S-H. We have identified two sites for the incorporation of octahedrally coordinated zinc oxyhydroxide species ($ZnO_2(OH)_2^{4-}$) into C-S-H. This was done experimentally at a Ca/Si ratio of 1.75 and explored between 1.25 and 2.25 with atomistic modeling. As mentioned above, the incorporation of small amounts of zinc in the hydration of the key cement phases leads to significant acceleration in hydration kinetics and accompanying increase in hardened strength.[5,11] Synthetic C-S-H systems generally show a thin sheet morphology (Figures 2B and S2), indicating that growth is mainly in the a–b directions and very limited along the c-axis. Three of the zinc sites are found in the silicate chains, which lie parallel to the b-direction. During the growth of C-S-H, the main silicate species in solution is the neutral complex $CaSiO_2(OH)_2$ (present at 2 mM concentrations).[62] To link these species to form the calcium silicate sheets that make up C-S-H, bridging species such as monomeric silicates (0.05 mM) or Ca^{2+} (10 mM) are needed. The main zinc species in solution is $ZnO_2(OH)_2^{4-}$ (2 mM) at the pH values used here and in cementitious systems.[48] Here, we have found that this species is readily incorporated into both the bridging position and the $Q^{(1)}$ end chain position and can hence accelerate the growth of C-S-H by simply increasing the number of growth units in solution. From ICP measurements of the supernatant (Figure S3), we see that even at a molar ratio of 0.4 Zn/Si, the vast majority (98–99%) of the zinc is incorporated into the C-S-H. Taking the ensemble of our observations together, we suggest the acceleration seen in hydration[4−6] could be due to the enhanced concentration of effective monomeric growth species (Zn ≫ Si) at the early stages of growth.

Additionally, $[(HO)_3ZnOSiO_2OH]^{4-}$ and $[(HO)_3ZnO(SiO_2)O(SiO_2)OH]^{6-}$ species have been postulated at pH

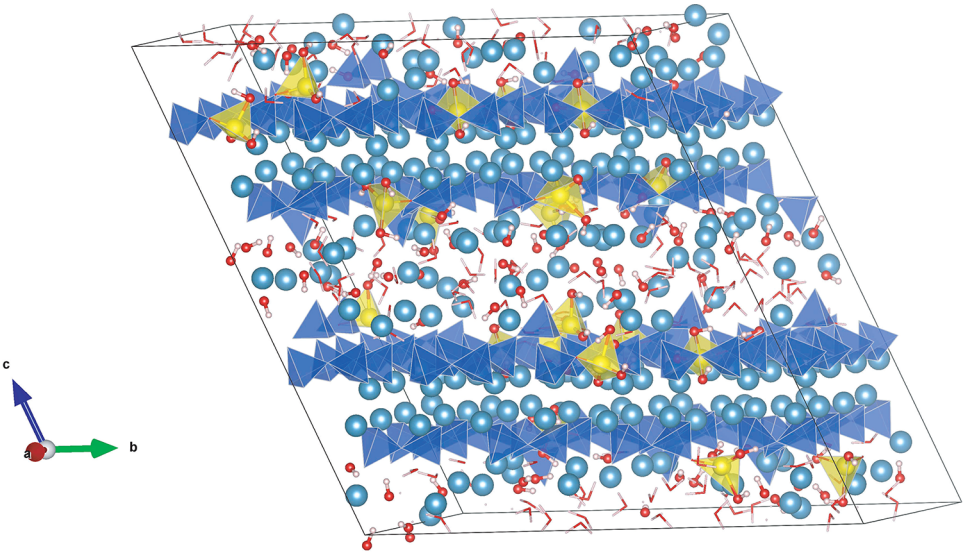

Figure 6. Representative atomic-level structure of zinc-modified C-S-H as determined with $(Zn/Si)_i = 0.15$. Silicate tetrahedra are depicted in blue; zincate tetrahedra are depicted in yellow; and calcium ions are depicted in light blue.

https://doi.org/10.1021/jacs.2c06749
J. Am. Chem. Soc. 2022, 144, 22915−22924

above 14, and they may also play a role in the chain formation process.[48]

To validate the hypotheses generated from the atomic-level structures of zinc-modified C-S-H determined here, detailed thermodynamic modeling and kinetic experiments on synthetic C-S-H in the presence of zinc will be carried out in future studies, for example, using the population balance approach developed by Andalibi et al.[62] to model both growth rates and monitor solution speciation as a function of the reaction time.

CONCLUSIONS

We precipitated pure single-phase C-S-H in the presence of zinc with a target Ca/Si ratio of 1.75, analogous to industrially relevant compositions, from a solution of aqueous sodium metasilicate, calcium nitrate, and zinc nitrate under controlled pH, temperature, and atmospheric conditions. TEM was used to observe the microstructure of the precipitated product, and EDX confirmed the local composition. DNP-enhanced 1D $^{1}H \rightarrow {}^{29}Si$ multi-CPMAS NMR was used to measure quantitative populations of Q species, and natural-abundance 2D ^{29}Si-^{29}Si INADEQUATE spectra were used to determine the connectivities between the silicate species.

These data, in combination with atomistic modeling and DFT chemical shift calculations, were used to determine the atomic-level structure of zinc-modified synthetic C-S-H.

Specifically, as shown in Figure 6, two new silicate sites are present in the structure: $Q^{(1,Zn)}$ and $Q^{(2p,Zn)}$. By determining the structure in three samples with different $(Zn/Si)_i$ ratios, we find that zinc promotes an increase of the mean chain lengths.

The structure suggests that the enhanced hydration kinetics in zinc-containing cementitious systems could be due to the enhanced concentration of effective monomeric species at the early stages of growth. Considering that real cementitious systems also contain aluminum and that aluminum is known to incorporate into the C-S-H structure, work is in progress to study the impact of dual incorporation of zinc and aluminum in C-S-H.

ASSOCIATED CONTENT

Supporting Information

The Supporting Information is available free of charge at https://pubs.acs.org/doi/10.1021/jacs.2c06749.

Experimental details, additional characterization data, structures, and link to the raw data (DFT output files of each structure investigated, LAMMPS input files, and NMR raw data) (PDF)

CIF files of the Zn-modified C-S-H structures (ZIP)

AUTHOR INFORMATION

Corresponding Authors

Karen L. Scrivener − *Laboratory of Construction Materials, Institut des Matériaux, Ecole Polytechnique Fédérale de Lausanne (EPFL), CH-1015 Lausanne, Switzerland*; Email: karen.scrivener@epfl.ch

Paul Bowen − *Laboratory of Construction Materials, Institut des Matériaux, Ecole Polytechnique Fédérale de Lausanne (EPFL), CH-1015 Lausanne, Switzerland*; Email: paul.bowen@epfl.ch

Lyndon Emsley − *Laboratory of Magnetic Resonance, Institut des Sciences et Ingénierie Chimiques, Ecole Polytechnique Fédérale de Lausanne (EPFL), CH-1015 Lausanne, Switzerland*; orcid.org/0000-0003-1360-2572; Email: lyndon.emsley@epfl.ch

Authors

Anna Morales-Melgares − *Laboratory of Magnetic Resonance, Institut des Sciences et Ingénierie Chimiques, Ecole Polytechnique Fédérale de Lausanne (EPFL), CH-1015 Lausanne, Switzerland; Laboratory of Construction Materials, Institut des Matériaux, Ecole Polytechnique Fédérale de Lausanne (EPFL), CH-1015 Lausanne, Switzerland*

Ziga Casar − *Laboratory of Construction Materials, Institut des Matériaux, Ecole Polytechnique Fédérale de Lausanne (EPFL), CH-1015 Lausanne, Switzerland*

Pinelopi Moutzouri − *Laboratory of Magnetic Resonance, Institut des Sciences et Ingénierie Chimiques, Ecole Polytechnique Fédérale de Lausanne (EPFL), CH-1015 Lausanne, Switzerland*

Amrit Venkatesh − *Laboratory of Magnetic Resonance, Institut des Sciences et Ingénierie Chimiques, Ecole Polytechnique Fédérale de Lausanne (EPFL), CH-1015 Lausanne, Switzerland*; orcid.org/0000-0001-5319-9269

Manuel Cordova − *Laboratory of Magnetic Resonance, Institut des Sciences et Ingénierie Chimiques, Ecole Polytechnique Fédérale de Lausanne (EPFL), CH-1015 Lausanne, Switzerland*; orcid.org/0000-0002-8722-6541

Aslam Kunhi Mohamed − *Institute for Building Materials, Department of Civil, Environmental and Geomatic Engineering, ETH Zürich, CH-8093 Zürich, Switzerland*; orcid.org/0000-0001-6680-9599

Complete contact information is available at: https://pubs.acs.org/10.1021/jacs.2c06749

Author Contributions

‖A.M.-M. and Z.C. contributed equally to this work. The manuscript was written through contributions of all authors. All authors have given approval to the final version of the manuscript.

Notes

The authors declare no competing financial interest.

ACKNOWLEDGMENTS

Financial support from the Swiss National Science Foundation Grant No. 200021_179076 is acknowledged. A.V. acknowledges H2020 Marie Skłodowska−Curie Individual fellowship (grant number 101024369). The authors would also like to thank Ayush Agarwal (PSI, Switzerland) for the ICP measurements.

REFERENCES

(1) Scrivener, K. L.; Kirkpatrick, R. J. Innovation in Use and Research on Cementitious Material. *Cem. Concr. Res.* **2008**, *38*, 128−136.

(2) Megat Johari, M. A.; Brooks, J. J.; Kabir, S.; Rivard, P. Influence of Supplementary Cementitious Materials on Engineering Properties of High Strength Concrete. *Constr. Build. Mater.* **2011**, *25*, 2639−2648.

(3) Juenger, M. C. G.; Siddique, R. Recent Advances in Understanding the Role of Supplementary Cementitious Materials in Concrete. *Cem. Concr. Res.* **2015**, *78*, 71−80.

(4) Stephan, D.; Maleki, H.; Knöfel, D.; Eber, B.; Härdtl, R. Influence of Cr, Ni, and Zn on the Properties of Pure Clinker Phases: Part I. C_3S. *Cem. Concr. Res.* **1999**, *29*, 545−552.

(5) Li, X.; Scrivener, K. L. Impact of ZnO on C_3S hydration and C-S-H Morphology at Early Ages. *Cem. Concr. Res.* **2022**, *154*, No. 106734.
(6) Odler, I.; Abdul-Maula, S. Polymorphism and Hydration of Tricalcium Silicate Doped with ZnO. *J. Am. Ceram. Soc.* **1983**, *66*, 1−4.
(7) Bullard, J. W.; Jennings, H. M.; Livingston, R. A.; Nonat, A.; Scherer, G. W.; Schweitzer, J. S.; Scrivener, K. L.; Thomas, J. J. Mechanisms of Cement Hydration. *Cem. Concr. Res.* **2011**, *41*, 1208−1223.
(8) Scrivener, K. L.; Juilland, P.; Monteiro, P. J. M. Advances in understanding hydration of Portland cement. *Cem. Concr. Res.* **2015**, *78*, 38−56.
(9) Scrivener, K.; Ouzia, A.; Juilland, P.; Kunhi Mohamed, A. Advances in Understanding Cement Hydration Mechanisms. *Cem. Concr. Res.* **2019**, *124*, No. 105823.
(10) Ouzia, A.; Scrivener, K. The Needle Model: A New Model for the Main Hydration Peak of Alite. *Cem. Concr. Res.* **2019**, *115*, 339−360.
(11) Bazzoni, A.; Ma, S.; Wang, Q.; Shen, X.; Cantoni, M.; Scrivener, K. L. The Effect of Magnesium and Zinc Ions on the Hydration Kinetics of C_3S. *J. Am. Ceram. Soc.* **2014**, *97*, 3684−3693.
(12) Nonat, A.; Lecoq, X.The Structure, Stoichiometry and Properties of C-S-H Prepared by C3S hydration under Controlled Condition. In *Nuclear Magnetic Resonance Spectroscopy of Cement-based Materials*; Springer, 1998; pp 197−207.
(13) Nonat, A. The Structure and Stoichiometry of C-S-H. *Cem. Concr. Res.* **2004**, *34*, 1521−1528.
(14) Klur, I.; Pollet, B.; Virlet, J.; Nonat, A.C-S-H Structure Evolution with Calcium Content by Multinuclear NMR. In *Nuclear magnetic resonance spectroscopy of cement-based materials*, Springer, 1998; pp 119−141.
(15) Kumar, A.; Walder, B. J.; Kunhi Mohamed, A.; Hofstetter, A.; Srinivasan, B.; Rossini, A. J.; Scrivener, K.; Emsley, L.; Bowen, P. The atomic-level structure of cementitious calcium silicate hydrate. *J. Phys. Chem. C* **2017**, *121*, 17188−17196.
(16) Kunhi Mohamed, A.; Moutzouri, P.; Berruyer, P.; Walder, B. J.; Siramanont, J.; Harris, M.; Negroni, M.; Galmarini, S. C.; Parker, S. C.; Scrivener, K. L.; Emsley, L.; Bowen, P. The Atomic-Level Structure of Cementitious Calcium Aluminate Silicate Hydrate. *J. Am. Chem. Soc.* **2020**, *142*, 11060−11071.
(17) Harris, M.; Simpson, G.; Scrivener, K.; Bowen, P. A Method for the Reliable and Reproducible Precipitation of Phase Pure high Ca/Si ratio (> 1.5) Synthetic Calcium Silicate Hydrates (C-S-H). *Cem. Concr. Res.* **2022**, *151*, No. 106623.
(18) Maddalena, R.; Hamilton, A. Low-pressure Silica Injection for Porosity Reduction in Cementitious Materials. *Constr. Build. Mater.* **2017**, *134*, 610−616.
(19) Renaudin, G.; Russias, J.; Leroux, F.; Frizon, F.; Cau-dit-Coumes, C. Structural Characterization of C−S−H and C−A−S−H Samples-Part I: Long-Range Order Investigated by Rietveld Analyses. *J. Solid State Chem.* **2009**, *182*, 3312−3319.
(20) Rossini, A. J.; Zagdoun, A.; Lelli, M.; Lesage, A.; Coperet, C.; Emsley, L. Dynamic Nuclear Polarization Surface Enhanced NMR Spectroscopy. *Acc. Chem. Res.* **2013**, *46*, 1942−1951.
(21) Lesage, A.; Lelli, M.; Gajan, D.; Caporini, M. A.; Vitzthum, V.; Miéville, P.; Alauzun, J.; Roussey, A.; Thieuleux, C.; Mehdi, A.; Bodenhausen, G.; Cóperet, C.; Emsley, L. Surface Enhanced NMR Spectroscopy by Dynamic Nuclear Polarization. *J. Am. Chem. Soc.* **2010**, *132*, 15459−15461.
(22) Rossini, A. J.; Zagdoun, A.; Hegner, F.; Schwarzwälder, M.; Gajan, D.; Copéret, C.; Lesage, A.; Emsley, L. Dynamic Nuclear Polarization NMR Spectroscopy of Microcrystalline Solids. *J. Am. Chem. Soc.* **2012**, *134*, 16899−16908.
(23) Sauvée, C.; Rosay, M.; Casano, G.; Aussenac, F.; Weber, R. T.; Ouari, O.; Tordo, P. Highly Efficient, Water-Soluble Polarizing Agents for Dynamic Nuclear polarization at high frequency. *Angew. Chem.* **2013**, *125*, 11058−11061.
(24) Ni, Q. Z.; Daviso, E.; Can, T. V.; Markhasin, E.; Jawla, S. K.; Swager, T. M.; Temkin, R. J.; Herzfeld, J.; Griffin, R. G. High Frequency Dynamic Nuclear Polarization. *Acc. Chem. Res.* **2013**, *46*, 1933−1941.
(25) Liu, S.-F.; Mao, J.-D.; Schmidt-Rohr, K. A Robust Technique for Two-Dimensional Separation of Undistorted Chemical-Shift Anisotropy Powder Patterns in Magic-Angle-Spinning NMR. *J. Magn. Reson.* **2002**, *155*, 15−28.
(26) van Meerten, S. G. J.; Franssen, W. M. J.; Kentgens, A. P. M. ssNake: A Cross-Platform Open-Source NMR Data Processing and Fitting Application. *J. Magn. Reson.* **2019**, *301*, 56−66.
(27) Kunhi Mohamed, A.; Parker, S. C.; Bowen, P.; Galmarini, S. An Atomistic Building Block Description of C-S-H-Towards a Realistic C-S-H Model. *Cem. Concr. Res.* **2018**, *107*, 221−235.
(28) Thompson, A. P.; Aktulga, H. M.; Berger, R.; Bolintineanu, D. S.; Brown, W. M.; Crozier, P. S.; in't Veld, P. J.; Kohlmeyer, A.; Moore, S. G.; Nguyen, T. D.; et al. LAMMPS-a Flexible Simulation Tool for Particle-Based Materials Modeling at the Atomic, Meso, and Continuum Scales. *Comput. Phys. Commun.* **2022**, *271*, No. 108171.
(29) Valavi, M.; Casar, Z.; Kunhi Mohamed, A.; Bowen, P.; Galmarini, S. Molecular Dynamic Simulations of Cementitious Systems Using a Newly Developed Force Field Suite ERICA FF. *Cem. Concr. Res.* **2022**, *154*, No. 106712.
(30) Lewis, G. V.; Catlow, C. R. A. Potential Models for Ionic Oxides. *J. Phys. C* **1985**, *18*, 1149−1161.
(31) Perdew, J. P.; Burke, K.; Ernzerhof, M. Generalized Gradient Approximation Made Simple. *Phys. Rev. Lett.* **1996**, *77*, 3865−3868.
(32) Grimme, S. Semiempirical GGA-Type Density Functional Constructed with a Long-Range Dispersion Correction. *J. Comput. Chem.* **2006**, *27*, 1787−1799.
(33) Barone, V.; Casarin, M.; Forrer, D.; Pavone, M.; Sambi, M.; Vittadini, A. Role and Effective Treatment of Dispersive Forces in Materials: Polyethylene and Graphite Crystals as Test Cases. *J. Comput. Chem.* **2009**, *30*, 934−939.
(34) Kresse, G.; Joubert, D. From Ultrasoft Pseudopotentials to the Projector Augmented-Wave Method. *Phys. Rev. B* **1999**, *59*, 1758−1775.
(35) Dal Corso, A. Pseudopotentials Periodic Table: From H to Pu. *Comput. Mater. Sci.* **2014**, *95*, 337−350.
(36) Monkhorst, H. J.; Pack, J. D. Special Points for Brillouin-Zone Integrations. *Phys. Rev. B* **1976**, *13*, 5188−5192.
(37) Pickard, C. J.; Mauri, F. All-Electron Magnetic Response with Pseudopotentials: NMR Chemical Shifts. *Phys. Rev. B* **2001**, *63*, No. 245101.
(38) Yates, J. R.; Pickard, C. J.; Mauri, F. Calculation of NMR Chemical Shifts for Extended Systems using Ultrasoft Pseudopotentials. *Phys. Rev. B* **2007**, *76*, No. 024401.
(39) Klaska, K.-H.; Eck, J.; Pohl, D. New Investigation of Willemite. *Acta Crystallogr. B: Struct. Sci. Cryst. Eng. Mater.* **1978**, *34*, 3324−3325.
(40) Hill, R. J.; Gibbs, G. V.; Craig, J. R. A Neutron-Diffraction Study of Hemimorphite. *Z. Kristallogr. Cryst. Mater.* **1977**, *146*, 241−259.
(41) Gard, J. A.; Taylor, H. F. W. The Crystal Structure of Foshagite. *Acta Crystallogr.* **1960**, *13*, 785−793.
(42) Smith, G. S.; Alexander, L. E. Refinement of the Atomic Parameters of [Alpha]-Quartz. *Acta Crystallogr.* **1963**, *16*, 462−471.
(43) Chandrappa, G. T.; Ghosh, S.; Patil, K. C. Synthesis and Properties of Willemite, Zn2SiO4, and M2+:Zn2SiO4 (M=Co and Ni). *J. Mater. Synth. Process.* **1999**, *7*, 273−279.
(44) Lippmaa, E.; Maegi, M.; Samoson, A.; Engelhardt, G.; Grimmer, A.-R. Structural Studies of Silicates by Solid-State High-Resolution Silicon-29 NMR. *J. Am. Chem. Soc.* **1980**, *102*, 4889−4893.
(45) Giannozzi, P.; Baroni, S.; Bonini, N.; Calandra, M.; Car, R.; Cavazzoni, C.; Ceresoli, D.; Chiarotti, G. L.; Cococcioni, M.; Dabo, I.; Dal Corso, A.; de Gironcoli, S.; Fabris, S.; Fratesi, G.; et al. QUANTUM ESPRESSO: a Modular and Open-Source Software

Project for Quantum Simulations of Materials. *J. Phys. Condens. Matter* **2009**, *21*, No. 395502.
(46) Giannozzi, P.; Andreussi, O.; Brumme, T.; Bunau, O.; Buongiorno Nardelli, M.; Calandra, M.; Car, R.; Cavazzoni, C.; Ceresoli, D.; Cococcioni, M.; Colonna, N.; Carnimeo, I.; Dal Corso, A.; de Gironcoli, S.; et al. Advanced Capabilities for Materials Modelling with Quantum ESPRESSO. *J. Phys. Condens. Matter* **2017**, *29*, No. 465901.
(47) Virtanen, P.; Gommers, R.; Oliphant, T. E.; Haberland, M.; Reddy, T.; Cournapeau, D.; Burovski, E.; Peterson, P.; Weckesser, W.; Bright, J.; et al. SciPy 1.0: Fundamental Algorithms for Scientific Computing in Python. *Nat. Methods* **2020**, *17*, 261−272.
(48) Anseau, M. R.; Leung, J. P.; Sahai, N.; Swaddle, T. W. Interactions of Silicate Ions with Zinc (II) and Aluminum (III) in Alkaline Aqueous Solution. *Inorg. Chem.* **2005**, *44*, 8023−8032.
(49) Tommaseo, C. E.; Kersten, M. Aqueous Solubility Diagrams for Cementitious Waste Stabilization Systems. 3. Mechanism of Zinc Immobilizaton by Calcium Silicate Hydrate. *Environ. Sci. Technol.* **2002**, *36*, 2919−2925.
(50) Rose, J.; Moulin, I.; Masion, A.; Bertsch, P. M.; Wiesner, M. R.; Bottero, J.-Y.; Mosnier, F.; Haehnel, C. X-Ray Absorption Spectroscopy Study of Immobilization Processes for Heavy Metals in Calcium Silicate Hydrates. 2. Zinc. *Langmuir* **2001**, *17*, 3658−3665.
(51) Johnson, R. L.; Schmidt-Rohr, K. Quantitative Solid-State ^{13}C NMR with Signal Enhancement by Multiple Cross Polarization. *J. Magn. Reson.* **2014**, *239*, 44−49.
(52) Fyfe, C. A.; Grondey, H.; Feng, Y.; Kokotailo, G. T. Natural-Abundance Two-Dimensional Silicon-29 MAS NMR Investigation of the Three-Dimensional Bonding Connectivities in the Zeolite Catalyst ZSM-5. *J. Am. Chem. Soc.* **1990**, *112*, 8812−8820.
(53) Lesage, A.; Bardet, M.; Emsley, L. Through-Bond Carbon-Carbon Connectivities in Disordered Solids by NMR. *J. Am. Chem. Soc.* **1999**, *121*, 10987−10993.
(54) Bertarello, A.; Berruyer, P.; Skantze, U.; Sardana, S.; Sardana, M.; Elmore, C. S.; Schade, M.; Chiarparin, E.; Schantz, S.; Emsley, L. Quantification of Magic Angle Spinning Dynamic Nuclear Polarization NMR Spectra. *J. Magn. Reson.* **2021**, *329*, No. 107030.
(55) Alonso, C.; Fernandez, L. Dehydration and Rehydration Processes of Cement Paste Exposed to High Temperature Environments. *J. Mater. Sci.* **2004**, *39*, 3015−3024.
(56) Sato, H.; Grutzeck, M. Effect of Starting Materials on the Synthesis of Tobermorite. *MRS Online Proc. Libr.* **1991**, *245*, 235−240.
(57) Hong, S. H.; Young, J. F. Hydration Kinetics and Phase Stability of Dicalcium Silicate Synthesized by the Pechini Process. *J. Am. Ceram. Soc.* **1999**, *82*, 1681−1686.
(58) Wang, L.; Geddes, D. A.; Walkley, B.; Provis, J. L.; Mechtcherine, V.; Tsang, D. C. W. The Role of Zinc in Metakaolin-Based Geopolymers. *Cem. Concr. Res.* **2020**, *136*, No. 106194.
(59) Brunet, F.; Bertani, P.; Charpentier, T.; Nonat, A.; Virlet, J. Application of ^{29}Si Homonuclear and $^{1}H-^{29}Si$ Heteronuclear NMR Correlation to Structural Studies of Calcium Silicate Hydrates. *J. Phys. Chem. B* **2004**, *108*, 15494−15502.
(60) Cong, X.; Kirkpatrick, R. J. ^{29}Si MAS NMR Study of the Structure of Calcium Silicate Hydrate. *Adv. Cem. Based Mater.* **1996**, *3*, 144−156.
(61) Pustovgar, E.; Sangodkar, R. P.; Andreev, A. S.; Palacios, M.; Chmelka, B. F.; Flatt, R. J.; d'Espinose de Lacaillerie, J.-B. Understanding Silicate Hydration from Quantitative Analyses of Hydrating Tricalcium Silicates. *Nat. Commun.* **2016**, *7*, No. 10952.
(62) Andalibi, M. R.; Kumar, A.; Srinivasan, B.; Bowen, P.; Scrivener, K.; Ludwig, C.; Testino, A. On the Mesoscale Mechanism of Synthetic Calcium−Silicate−Hydrate Precipitation: a Population Balance Modeling Approach. *J. Mater. Chem. A* **2018**, *6*, 363−373.

https://doi.org/10.1021/jacs.2c06749
J. Am. Chem. Soc. 2022, 144, 22915−22924